

Automated GPR Rebar Analysis for Robotic Bridge Deck Evaluation

Parneet Kaur, Kristin J. Dana, Francisco A. Romero, and Nenad Gucunski

Abstract—Ground penetrating radar (GPR) is used to evaluate deterioration of reinforced concrete bridge decks based on measuring signal attenuation from embedded rebar. The existing methods for obtaining deterioration maps from GPR data often require manual interaction and offsite processing. In this paper, a novel algorithm is presented for automated rebar detection and analysis. We test the process with comprehensive measurements obtained using a novel state-of-the-art robotic bridge inspection system equipped with GPR sensors. The algorithm achieves robust performance by integrating machine learning classification using image-based gradient features and robust curve fitting of the rebar hyperbolic signature. The approach avoids edge detection, thresholding, and template matching that require manual tuning and are known to perform poorly in the presence of noise and outliers. The detected hyperbolic signatures of rebars within the bridge deck are used to generate deterioration maps of the bridge deck. The results of the rebar region detector are compared quantitatively with several methods of image-based classification and a significant performance advantage is demonstrated. High rates of accuracy are reported on real data that includes thousands of individual hyperbolic rebar signatures from three real bridge decks.

Index Terms—Automatic rebar detection, depth correction, ground penetrating radar (GPR), histogram of oriented gradients (HOG), hyperbolic signature, machine learning, pattern recognition, robotic bridge inspection, robust curve fitting, support vector machines (SVM).

I. INTRODUCTION

BRIDGES deteriorate with time due to factors like aging, changing weather conditions, increased traffic load and use of de-icing salts. Reinforced concrete (RC) bridges have steel bars, called rebars, which are embedded within the decks for structural strength (Fig. 1). Rebars are prone to corrosion due to moisture and chloride ions from the use of

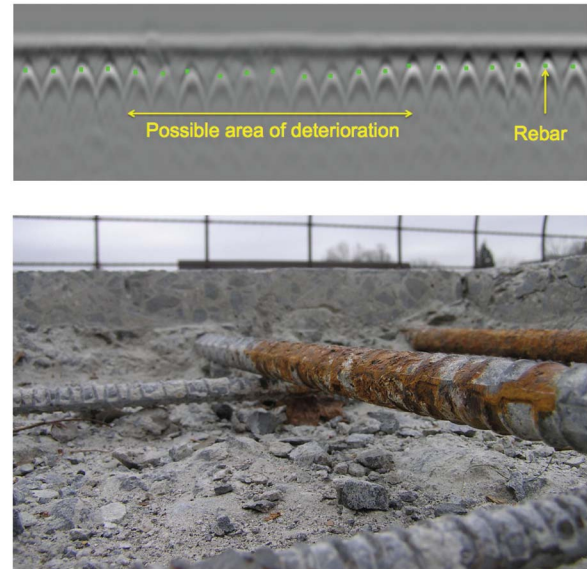


Fig. 1. Top row: example result of automatic detection of underground rebars using our algorithm. The peak amplitude near the hyperbolic signature is marked and an area of possible deterioration is evident. Bottom row: exposed rebar where corrosion has occurred over time due to moisture and chloride ions. GPR is used to analyze rebar integrity without excavation.

deicing salts. Measures are taken to prevent rebar corrosion by applying resistant coating, incorporating inhibitors in concrete and providing adequate concrete cover [1]. However, these measures only delay the process. Moreover, once passive protection around rebars is compromised, accelerated corrosion can take place. By the time the effect of rebar damage is visible on the surface of bridge deck in form of cracks accompanied by rust stains, extensive deterioration has already taken place. Since rebars are embedded and not accessible to physical measurement at the surface, obtaining an accurate condition assessment of deteriorated areas can be challenging.

Traditional methods like half-cell potential test, chain drag, and coring are labor intensive and require access to the bare concrete surface or drilled holes [2], [3]. On the other hand, employing nondestructive test (NDT) methods is less labor intensive and facilitates faster data collection. Ground penetrating radar (GPR) is one of the most widely used NDT methods for detecting subsurface anomalies in concrete cover [4]–[6]. In bridge surveys, GPR is used to measure concrete thickness, estimate relative water moisture content variation and mark or map rebar locations, as well as to provide corrosion-based

Manuscript received March 25, 2014; revised March 12, 2015 and June 23, 2015; accepted August 17, 2015. Date of publication October 26, 2015; date of current version September 14, 2016. This work was supported by the Federal Highway Administration's Long Term Bridge Performance Program at Rutgers Center for Advanced Infrastructure and Transportation. This paper was recommended by Associate Editor Y. Tan.

P. Kaur and K. J. Dana are with the Department of Electrical and Computer Engineering, Rutgers University, Piscataway, NJ 08854 USA (e-mail: parneet@rutgers.edu; kdana@ece.rutgers.edu).

F. A. Romero is with Romero NDT&E, LLC, Glen Gardner, NJ 08826 USA (e-mail: Francisco@RomeroNDTE.com).

N. Gucunski is with the Center for Advanced Infrastructure and Technology, Rutgers University, Piscataway, NJ 08854 USA (e-mail: gucunski@rci.rutgers.edu).

The dataset for the Warren County Bridge, NJ is available at: https://github.com/kjdana/automated_rebar_analysis_dataset.

Color versions of one or more of the figures in this paper are available online at <http://ieeexplore.ieee.org>.

Digital Object Identifier 10.1109/TCYB.2015.2474747



Fig. 2. GPR data for rebar inspection are acquired by a novel robotic system for automated bridge inspection: robotics assisted bridge inspection tool.

condition assessments of RC decks. The information captured by GPR can be represented as high quality images that can be analyzed directly using pattern recognition and machine learning methods. Recent methods for robotic bridge deck scanning [7] provides densely sampled and repeatable bridge measurements. Densely sampled measurements can also be obtained with mobile trailers [8] and wheeled carts equipped with GPR sensors [9].

Many of the existing methods for processing GPR data require manual input and are suitable primarily for interactive offsite analysis [10]. With the advent of robotic and mobile bridge scanning, measurement sets are large and there is a need for on-site data analytics. Semi-automated analysis methods requiring manual input is prohibitively time-consuming and cumbersome for large datasets. Data acquisition is readily achievable with mechanical robotics, fast sensors, and portable storage devices; however, extracting knowledge from vast measurements in an efficient manner is still a challenge. This paper provides a novel method for automatic detection and localization of rebars from GPR data for deterioration analysis. The approach is tested using measurements from a state-of-the-art robotic bridge scanner [7] as shown in Fig. 2. The algorithm is designed and evaluated for rebar detection on large regions of real bridge decks and provides demonstrable advantages over prior methods for GPR rebar detection. We test the process with comprehensive measurements at the following three bridge decks: 1) U.S. Route 15 James Madison Highway, Haymarket, VA; 2) 150 Municipal Dr. Bloomsbury, Warren County, NJ; and 3) Slab section at Rutgers University, Livingston Campus, New Brunswick, NJ.

A. Background and Related Work

In much of the literature, GPR sensor output can be treated as images which exhibit a hyperbolic signature as discussed in detail in Section II. The image-based approach is less computationally intensive than the inverse scattering problem [11] because pattern analysis is done for a local region of the bridge deck. An intuitive approach used often in [12]–[16] is to

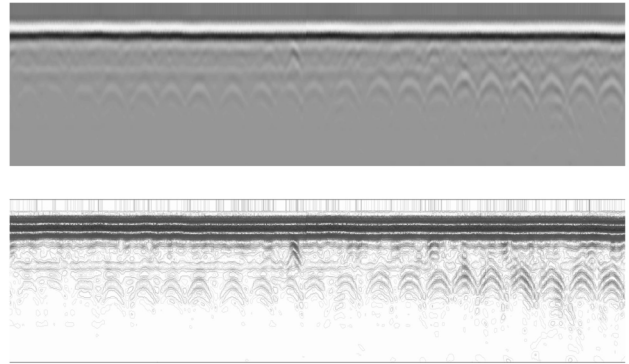


Fig. 3. Top row: GPR-scan from a real bridge. Bottom row: edge information. Notice the edges do not trace the perceived hyperbola and are susceptible to noise and other artifacts.

use edge detection, or thresholding on local extrema of intensity, to preprocess the image and isolate potential hyperbola regions. Edge detection has well known limitations including poor performance in the presence of noise and image blurring. Additionally, the thresholding typically requires one or more manually selected parameters that must be tuned to a given dataset. An example of the problems of edge detection in preprocessing is illustrated in Fig. 3.

Another simple approach to detect rebar regions that has been used in prior work is template matching with normalized cross-correlation as the matching criterion for invariance to intensity changes [9], [17], [18]. Template matching as a main step or a preprocessing step has significant limitations. In particular, the appearance of the hyperbola can vary from bridge to bridge due to variation in concrete type, rebar depth and noise. Additionally, a threshold must be chosen manually by experimentation. Methods such as [17] use template matching as a preprocessing step, followed by a hyperbolic curve fitting using partial differential equations. As shown in Fig. 4, template matching can cause many missing and false detections.

Edge detection, thresholding, and template matching are not appropriate for robust performance in large real-world datasets. These issues have been well studied in the computer vision literature and modern methods incorporate machine learning. Specifically, supervised learning yields high-classification accuracy by using a training phase with labeled examples to eliminate the need for parameter tuning. For automated GPR rebar detection, the machine learning method of neural networks has been applied [14], [15], [19]–[21]. These methods [14], [15], [19] use edge detection as a preprocessor and therefore have the same general limitations with respect to noise and parameter tuning that compromise edge detectors. Singh and Nene [21] showed promise using neural nets in the classification stage, but the results are limited to a single GPR image with four hyperbolas. Trapezoidal cropping of the image region before neural net classification is performed in [20], and hyperbolic regions can be detected. However, no curve fitting is provided and the hyperbola apex is coarsely localized by pixel evaluation in the fixed trapezoidal region. Another approach in automated rebar classification uses support vector machines (SVM) [22], [23]. Prior work in SVM

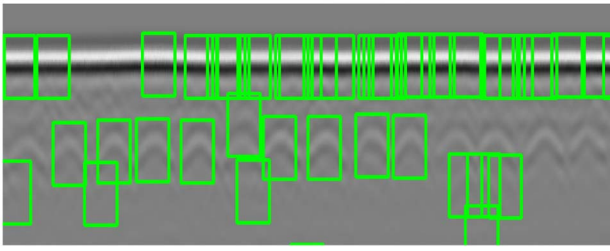


Fig. 4. Template matching with normalized cross-correlation results in many missing and false detections.

rebar detection [24] shows good results albeit with synthetic data. Unfortunately, a thresholding step is used to binarize the image, creating a fragile image representation that depends strongly on parameter selection. While our method also uses SVM, we do not require a thresholding step and therefore avoid the manually defined threshold parameter.

Curve fitting is an important component in identifying true hyperbolic signatures and locating them precisely. This localization is important so that the amplitude data at the true peak can be recorded and compared over time to detect deterioration. Examples of prior work that include hyperbolic curve fitting include [12], [17], [25]; however, edge detection is used as a preprocessing step in [12] and results for only one hyperbolic signature is given in [25]. Template matching is the preprocessing step in [17]. Furthermore, no region of interest detection is included and no outliers are handled in the curve fitting algorithm.

In much of the prior literature, results are shown on either few examples, synthetic data, or simulated real data. For example, the approach in [14] successfully detects rebars by finding overlapping sections of hyperbolic edges on GPR scans obtained from an emulsion analogue tank simulating concrete properties. The concrete specimens have small physical dimensions (300×1200 mm with 16 mm diameter rebar) and do not exhibit the same appearance variability as real-bridge rebars. In general, the problems of edge detection, thresholding and template matching become evident when the data moves to large sets and real data. Since no prior work shows the compiled results on thousands of hyperbola signatures, our testing framework is the most extensive to date.

Machine learning methods that require training should be arranged with training data and test data from different geographic locations. With this approach, the system can be trained once and used subsequently at other locations without training or parameter tuning. This concept of mutually exclusive bridge decks is essential for assuring that the classification algorithm generalizes, but is not generally addressed in the prior work. Our methods represent a new paradigm in on-site data analytics using robotic data collection followed by automated rebar detection, localization, and evaluation.

In literature, the use of GPR scans for assessing rebar integrity has been validated by extracting rebar samples (cores) from the concrete bridge decks [26]. The cores are extracted from representative deteriorated and nondeteriorated locations based on the deterioration map obtained from analyzing GPR scans. The deterioration levels of the cores extracted

from these locations are in agreement with those indicated by the deterioration maps. This establishes that the analysis of hyperbolic signatures in the GPR scans reveals areas with corrosion-induced rebar deterioration. Apart with the corrosion, variation in the depth of the rebars in a bridge deck also decreases the signal strength (amplitude). So, it is important to apply a procedure depth-correction to minimize the effect of rebar depth such that the overall amplitude variation in the entire bridge deck is only indicative of corrosion. For the validation of rebar analysis using the proposed methods, we compare the deterioration maps obtained using our automated algorithm and Geophysical Survey Systems Inc. (GSSI) RADAN software [27], which involves manual interaction for localizing hyperbolic signatures. Traditionally, depth-correction is applied manually on the maps obtained by the RADAN software.

Our rebar analysis algorithm as depicted in Fig. 8, is not a trivial combination of existing parts, but rather each component has been carefully designed and tested for robust performance on rebars that vary in appearance due to differences in their structural properties. In order to evaluate various algorithm possibilities, the classification component has been evaluated with a suite of possible pattern matching methods including edges, intensity histograms, template matching, and the histogram of oriented gradients (HOG). A comparison of these methodologies for rebar detection as shown in Table V has not been addressed in prior work.

In summary, we present the first algorithm for GPR rebar detection that advances the state-of-the-art with the following key contributions: 1) machine learning classification to first detect rebar regions requiring no thresholding or edge detection; 2) robust curve fitting that can handle outliers and localize rebars within the region; and 3) a demonstration of results on a large set of real-bridge deck data (mutually exclusive from the training set) collected with a robotic bridge inspection system.

II. IMAGE FORMATION WITH GROUND PENETRATING RADAR

GPR has a well-established long-term role in assessing concrete bridges [28]–[33]. We summarize the basic operating principles in image formation. A ground-coupled antenna is used for this research as it provides images with more details for analysis than an air-coupled antenna. GPR systems consist of a transceiver in its antenna housing. The transmitter rapidly emits electromagnetic (EM) pulses at each measurement location and the receiver collects the reflected pulses as GPR raw-data. The time taken by an EM pulse to reach the target and then to the GPR receiver is called two-way travel time. The signal amplitude recorded on the acquisition unit as a function of two-way travel time is called an A-scan [Fig. 5(a)]. The positive and negative signal amplitudes are represented using a gray-scale color table. A-scans collected in a swath when the GPR is moving are stacked horizontally and called a B-scan or a radargram [Fig. 5(b)]. The number of A-scans to be collected per feet can be configured using the acquisition software. The B-scan is an image with the vertical axis showing two-way travel time of EM pulses and the

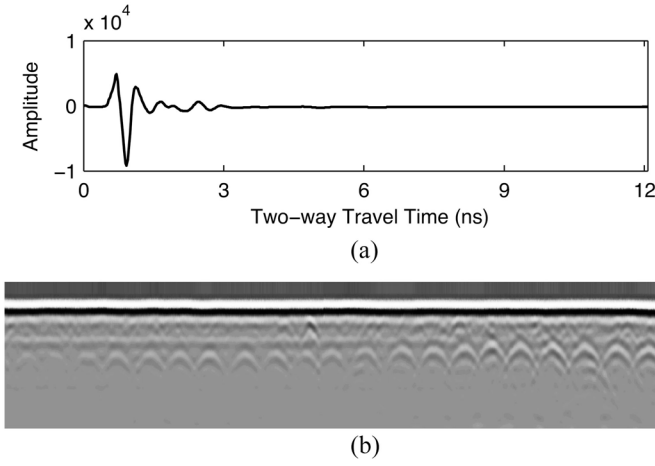


Fig. 5. (a) A-scan recorded by acquisition software at each measurement location. (b) A-scans collected in a swath when the GPR is moving are stacked horizontally and called a B-scan or a radargram.

horizontal axis representing the scan count or distance. Fig. 6 illustrates the data collection on a bridge and corresponding B-scans for each swath.

The signal strength of reflections from the subsurface material varies depending on its material properties. Relative dielectric properties of adjacent materials through which EM waves travel determine reflection strength of the signal. EM waves generated by a GPR system travel through concrete in bridge decks and are reflected from rebars, voids and other objects and anomalies of different dielectric properties. Strong reflections are observed at the rebar location and the concrete surface (Fig. 6).

For RC bridge decks, a GPR system is deployed so that the antenna scans the bridge in the direction perpendicular to the shallowest rebar. A GPR antenna transmits a wide beam which is reflected by the rebar exactly below the antenna and, if spaced closely enough at the given rebar depth, often the antenna will receive weaker (apparently deeper) signals from the neighboring rebars. A strong signal is observed when the GPR is directly above a rebar and diminishes as the antenna moves away from the rebar. The two-way travel time for the rebar reflection is minimum when the antenna is directly above the rebar and increases as antenna moves away from rebar.

As shown in Fig. 7, at location B [12]

$$d^2 = R_d^2 + X^2 \quad (1)$$

where d is distance traveled by the EM wave when GPR antenna is at location B , R_d is rebar depth (the distance traveled by the EM wave when the GPR antenna is directly above the rebar at location A), and X is the GPR spatial position.

The distances traveled by the EM wave at locations A and B are given, respectively, by

$$R_d = v \times \frac{t_A}{2} \quad (2)$$

and

$$d = v \times \frac{t_B}{2} \quad (3)$$

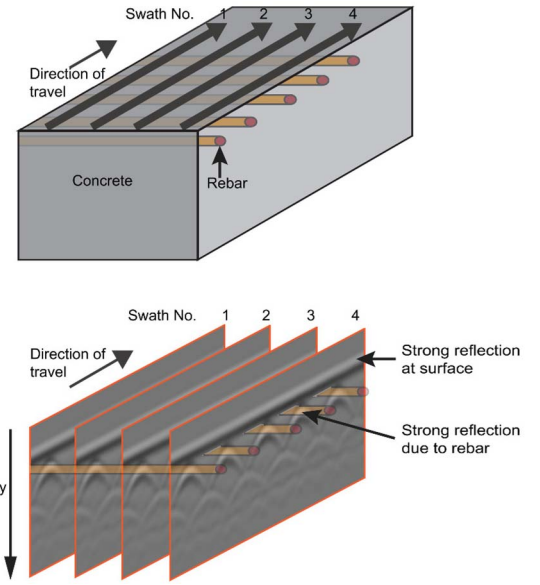


Fig. 6. Data collection using GPR. Data is collected along parallel lines, in direction perpendicular to rebars. This figure shows four parallel swaths for a small portion of bridge. Data collected in each swath is represented as a B-scan. Strong reflections are observed in a B-scan when EM waves travel from air to concrete or from concrete to rebar. Note that rebars form a distinct hyperbolic signature in a B-scan. Only partial B-scans are shown here.

where v is velocity of propagation of EM wave, t_A and t_B are two-way travel time at locations A and B .

Equations (1)–(3) can be combined as

$$\frac{t_B^2}{t_A^2} - 4 \frac{X^2}{(vt_A)^2} = 1 \quad (4)$$

which is the equation of a hyperbola. Thus, a distinct hyperbolic signature is formed for each rebar in a B-scan.

The B-scans are analyzed to find the rebar locations by identifying the strongest positive signal formed at the peak of hyperbola, which occurs when the antenna is exactly above a rebar. If rebar depth is constant throughout the bridge, the strength of the signal is indicative of the condition at the concrete rebar interface. The areas of the bridge deck, which are corroded or host a corrosive environment, have high-electrical conductivity due to presence of moisture and chloride ions. Due to increased electrical conductivity in chloride-laden environment within concrete most of the GPR signal is dispersed resulting in most of the attenuation in signal reflections from corroded regions of a bridge deck. In addition, the reduction in the dielectric contrast due to corroded rebars or moisture also contributes to some weakening of the signal reflections. Traditionally, the regions with lower amplitude indicate the possible corroded regions in a bridge deck.

The raw GPR data collected by the acquisition software needs to be preprocessed. The A-scans collected across the bridge may have a dc-offset because of receiver characteristics, which results in artifacts in the B-scan. The effect of dc-offset is removed by applying a moving average filter for each A-scan. The resultant data is then mapped linearly to gray-scale B-scan images.

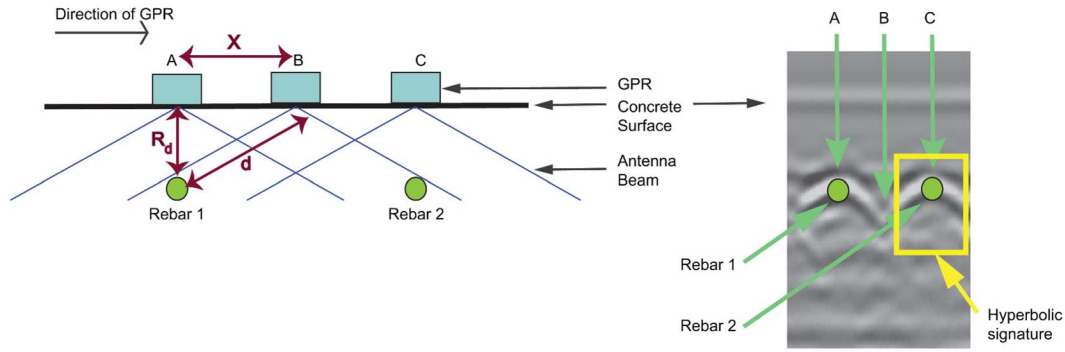


Fig. 7. Hyperbola signature for rebars. At location A, GPR is directly above Rebar 1 and the two-way travel-time of the signal reflected from rebar is minimum. As GPR moves away from Rebar 1, travel-time of reflected signal from rebar increases. At location B, GPR is between Rebars 1 and 2 and receives signals from both rebars and has greater two-way travel-time. As GPR moves toward Rebar 2, travel-time starts decreasing again and reaches minimum value at location C.

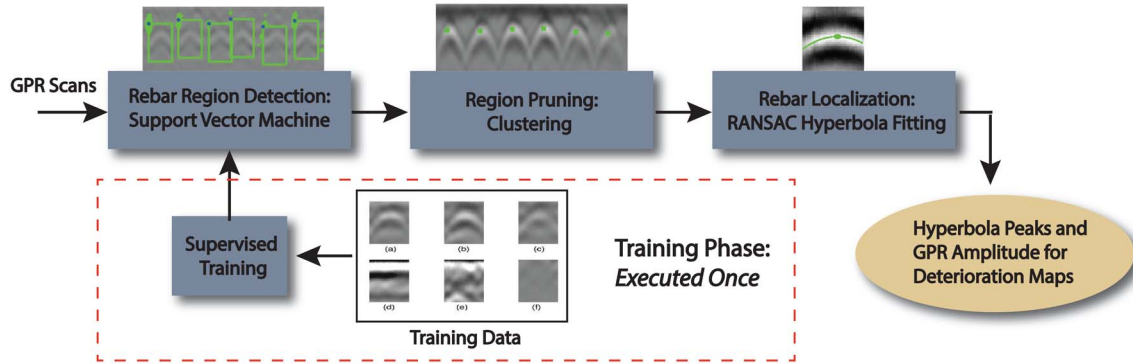


Fig. 8. Rebar detection and localization algorithm. The detection phase finds candidate rebar regions using SVM classification with HOG features. Multiple overlapping candidate regions are pruned to obtain spatially separate regions. During the localization phase a robust hyperbolic curve fit identifies the hyperbola location and parameters. The training phase to create the classifier is executed once and used for subsequent rebar detection.

III. METHODS

To compute deterioration maps from B-scan images, the first step is to detect the rebar regions and fit hyperbola in each such region to find the exact rebar location and its signal amplitude. Our automatic rebar detection algorithm (Fig. 8) starts with a rebar detection phase where candidate rebar regions are automatically selected using machine learning classification. Feature selection for the region descriptor is a key contribution of our approach. Redundant regions are detected because slightly shifted patches also are classified as rebar regions. Region pruning by clustering retains nonoverlapping region. Finally, the localization phase uses robust curve fitting to precisely determine the hyperbolic signature. Robust-fitting can localize the hyperbolic curve even in the presence of outliers and is an important algorithmic component.

A. Training Phase

During the training phase, an SVM classifier is constructed via optimization over a training dataset that has been assigned class labels. The classifier can then be used to predict labels of the unseen data (test set) that were not used for training. The training phase occurs only once and then the classifier is reused in subsequent rebar detection. An important aspect of this paper is that the training phase uses data from

a single real-world bridge deck, while the resultant classifier is applied to two additional geographic bridge locations. In this sense, the generalization of the classifier to unseen locations is demonstrated. These datasets and the classifier performance are discussed in Section IV. The concrete cover on the top rebar mat generally varies between 2 to 4 In. Within a bridge, the position of the rebars can vary from few millimeters to centimeters. The rebar diameter generally varies between 13 or 16 mm. Because of these standards in laying rebars, we expect similar hyperbolic signatures for different bridges. However, if there is a lot of variation in the depth or diameter of the rebars in a test set, the hyperbolic signatures will vary. In that case, the SVM classifier can be trained on one section of the bridge and tested on rest of the bridge.

Training an SVM classifier requires both positive and negative samples, i.e., regions with rebar hyperbolas are the positive samples and the remaining regions are negative samples as illustrated in Fig. 9. To train the classifier, features are computed from the manually labeled training data and the best separating hyperplane in feature space is computed. A fixed sample size of 52×32 pixels is used. Based on our comprehensive empirical investigation of a suite of candidate feature vectors described in Section IV, we show that the HOG [34]–[39] has the best performance for detecting hyperbolic regions in bridge deck regions. These features are only a component of our overall algorithm; they are used

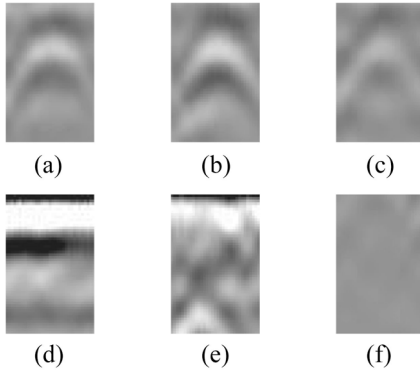


Fig. 9. (a)–(c) Positive samples. (d)–(f) Negative samples. Each sample is of size 52×32 pixels.

to train and then classify rebar regions but do not precisely localize the hyperbola within the resultant regions.

HOG represents the shape of the object to be detected by computing a dense grid of local gradients (edge directions) in an image [34], [35], [40]–[44]. The input image is divided into cells and an orientation based histogram of gradients with bin size (oBin) is computed for each cell using gradient orientation at each of its pixel. The cell histograms are normalized over spatially connecting block of size (sBin \times sBin), separately for each block. Normalizing the histogram improves the performance and makes the final descriptor invariant to contrast or illumination. The HOG implementation used in our experiments uses four different block normalizations (L2-norm, L2-norm followed by clipping, L1-norm, L1-norm square root). Normalized oriented gradients from the cells of all the spatially connecting blocks using each block normalization method are concatenated to construct a feature vector. We found that using only L2-norm normalization results in good classification results. We choose sBin = 5 and oBin = 10 empirically for our experiments.

HOG feature vector is insensitive to scale as long as the aspect ratio of hyperbolic signature remains constant. For a larger hyperbolic signature block size will increase (for fixed sBin and oBin) so the gradients are computed for more number of pixels in each block. However, the block normalization makes the final feature descriptor scale invariant for fixed aspect ratio of hyperbolic signatures. If the hyperbolic signature in test data is larger, the user needs to update the size of the search window in B-scans. However, since for the GPR parameters are fixed, we do not expect the hyperbolic signature size to vary a lot. As with any computer vision algorithm, if the test data is incomparable to the training data, the training will need to be performed again.

B. Rebar Detection

The trained classifier can be used to detect rebar regions in a B-scan. A moving window is moved one pixel at a time from top to bottom and left to right to extract a sample. Each sample is classified as a positive or negative sample. Rebar detection results obtained using HOG feature vectors are compared with a set of five additional feature vectors:

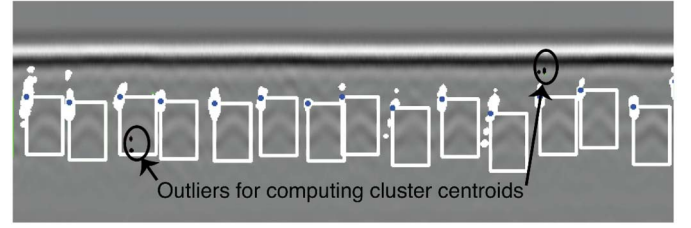


Fig. 10. Rebar region detection using HOG feature vectors. There are multiple candidate regions as indicated by the multiple dots marking the upper left corner of each candidate region. The cluster centroid is at the corner of the final rebar region (rectangle). Outliers 3σ in distance from the cluster groups are removed before centroid calculation.

1) direct gradient-orientation histogram; 2) maximum gradient orientation; 3) edge pixels; 4) intensity values; and 5) intensity histograms. In direct gradient-orientation histogram, each sample is divided into blocks to compute gradient-orientation histogram for each individual block and all the histograms stacked together are used as a feature vector. For our measurements, a block size of 8×4 is used. This feature vector is different from HOG descriptors since it does not weight the contributions based on gradient magnitude. For maximum gradient orientation each sample is divided into blocks, a gradient-orientation histogram is computed per block, and the bin with maximum histogram value is selected. For all blocks, the maximum gradient orientation bins are stacked together to form a feature vector. The edge-pixel feature vector is obtained by computing edge pixels in the blocks and stacking the binary edge image as a feature vector. The HOG feature performance is also compared with two simple intensity-based feature vectors. The feature from intensity values is the raw intensity values of each sample stacked as a single column vector [45], and the intensity histogram feature bins the raw intensity values in 25 intensity bins.

C. Rebar Region Pruning

When the moving window is directly over the distinct hyperbolic signature, the region is classified as a potential rebar region. However, when the window is moved by one pixel, the feature vector is essentially the same. The result is a cluster of positive samples, with the hyperbolic signature at its center as illustrated in Fig. 10. To identify a single rebar region for each hyperbolic signature, the centroid of each such cluster is computed. To fine-tune the cluster centroid, the points that are very far from the cluster centroid are identified as outliers. The distance of each point from the cluster centroid is computed and their mean (μ) and variation (σ) are recorded. A point is considered an outlier when its distance from centroid satisfies the condition

$$d > \mu + 3\sigma \quad (5)$$

where d is the distance of a point from cluster centroid, μ is the cluster mean, σ is the cluster variation. The centroid is computed again using the remaining points. Fig. 10 shows the rebar regions detected using cluster centroids.

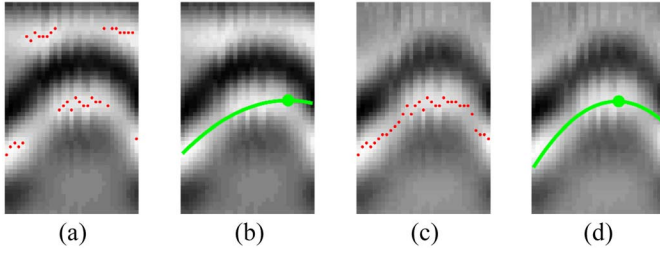


Fig. 11. Hyperbola fitting in presence of few outliers using RANSAC. (a) Input points for hyperbola fitting (red dots). (b) Hyperbola fitting using non-linear curve fitting. (c) Input points for hyperbola fitting using RANSAC (red dots). (d) Hyperbola fitting using RANSAC and non-linear curve fitting. By using RANSAC, hyperbola fitting improves and peak (green dot) is found correctly.

D. Rebar Localization

In each rebar region, hyperbolic curve fitting a hyperbola enables exact localization of the rebar through identifying the hyperbola peak. From the formation of hyperbola signatures from the A-scans, the maximum intensity points in each column form a hyperbola. These points are used as input points for fitting a north-south opening hyperbola of the form

$$\frac{(y-k)^2}{b^2} - \frac{(x-h)^2}{a^2} = 1 \quad (6)$$

where (h, k) is the center of hyperbola, a is length of semi-major axis, b is length of semi-minor axis. The input points used for hyperbola fitting can have outliers due to noise and unwanted subsurface reflections [Fig. 11(a)]. Using nonlinear curve fitting alone results in skewed hyperbola fitting in the presence of noise or outliers as illustrated in Fig. 11(b). Random sample consensus (RANSAC) [46], [47] is an iterative method that can be used for robust fitting in presence of outliers. The distance threshold between a data point and the hyperbola model used to decide if a data point is an inlier or outlier is 1.5. The maximum number of iterations allowed for converging to the model is 1000. Using RANSAC, hyperbola fitting is corrected as shown in Fig. 11(c).

E. Deterioration Maps From Hyperbolas

Detected rebars using the methods described in Sections III-A and III-D provide rebar location, two-way travel time and amplitude at each rebar location. The amplitude can be normalized against the maximum possible amplitude (32 768 for 16-bit data) and represented in decibels. If a contour plot based on normalized amplitudes at rebar locations is drawn, the rebars with attenuated amplitude will be shown as deteriorated areas. For corroded rebars, electrical conductivity of the rebars increases resulting in decreased velocity and increased two-way travel time of the EM waves. In addition to rebar corrosion, rebar depth also contributes to the attenuation of reflected signal. Since the two-way travel time is more for deeper rebars, they have attenuated signal reflections as compared to the signal reflection at shallow rebars.

To obtain a correct deterioration map, the effect of rebar depth must be removed so that amplitude variation is indicative of corrosion. A procedure called depth-correction is

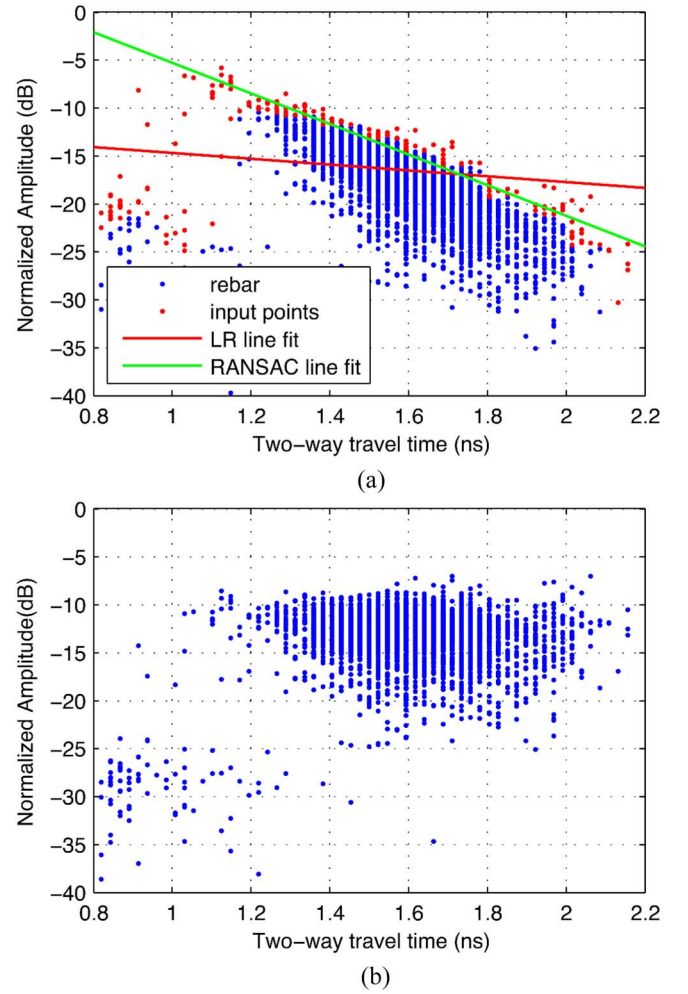


Fig. 12. Depth correction: each point corresponds to a rebar. (a) Depth versus amplitude plot for all rebars in the bridge. The RANSAC line fit is better than linear regression line fit in presence of outliers. (b) Depth correction applied to all the rebars.

applied [48], [49], where linear regression is used to find best-fit line to the 90th percentile value of normalized amplitudes at every measured value of two-way travel time [48]. Rebar amplitudes are corrected such that all the points along the best-fit line have the same amplitude. Fig. 12(a) shows a plot of normalized rebar amplitude versus time. The RANSAC line fit is through the rebars, where for different time (and hence, depth) there is variation in amplitudes. The distance threshold between a data point and the line-fitting model used to decide if a data point is an inlier or outlier is 0.5. The maximum number of iterations allowed for converging to the model is 1000. Fig. 12(b) shows a plot of normalized rebar amplitude versus time obtained after compensating for the variation in amplitudes due to time (depth).

IV. RESULTS

A. Data Collection and Experimental Setup

GPR data was collected using the robot bridge inspection system [7] and the IDS RIS Hi-Bright GPR (IDS Corporation) or with the GSSI SIR-20. IDS RIS Hi-Bright was used to collect data from two bridges A and B, listed in

TABLE I
DATA COLLECTION

| Bridge | Location |
|--------|--|
| A | US Route 15 (James Madison Highway), Haymarket, VA |
| B | 150, Municipal Dr., Bloomsbury, Warren County, NJ |
| C | Slab constructed at Livingston Campus, New Brunswick, NJ |

TABLE II
DATASETS FOR TRAINING, CROSS-VALIDATION, AND TESTING

| Dataset | Bridge | Positive samples | Negative samples |
|----------------------|--------|------------------|------------------|
| Training set | A | 1200 | 1200 |
| Cross-validation set | A | 300 | 300 |
| Test set B | B | 1000 | 1000 |
| Test set C | C | 1000 | 1000 |

Table I. In addition, it was also used to collect data from a concrete slab, which is referred to as bridge *C*. This slab was designed for automated nondestructive evaluation and rehabilitation system project at Rutgers University and has artificial delamination. GSSI SIR-20 was used to collect data from Bridges *B* and *C*. For both the acquisition units, 60 scans per foot are collected and each scan has 512 measurements spanning a time range of 12 ns.

To train and test the SVM classifier, datasets are constructed by extracting samples of size 52×32 pixels from the B-scans collected. Each sample is manually labeled as a positive or negative sample. Datasets are listed in Table II. The training set (2400 samples) and cross-validation set (600 samples) are constructed from bridge *A*. Once an SVM classifier is trained using the training data, it can be used to test data from any bridge. To test the trained classifier, two test sets are constructed from Bridges *B* and *C* with 2000 samples each. All sets have equal number of positive and negative samples. The hyperbolic signatures used for training and testing the SVM classifier are extracted from B-scans in a semi-automated way. First, we use template matching to detect and save the hyperbolic regions (52×32 pixels). The template is selected manually from one of the B-scans of the bridge. As shown in Fig. 4, template matching results in many positive and false-positive (FP) samples. These hyperbolic signatures are assigned one of the class labels: 1) positive (hyperbolic) samples or 2) negative (not hyperbolic) samples. Additionally, the hyperbolic regions which are not detected [false-negatives (FN)] by the template matching algorithm are extracted manually by cropping the image and labeled as the positive samples. Random samples from B-scans are also extracted and assigned one of the class labels.

B. Classifier Feature Selection

The SVM classifier trained using HOG feature vectors from training samples is used to classify cross-validation and test sets samples. In the training set and cross-validation set, all the samples are classified correctly and the accuracy is found to be 100%. For test sets *B* and *C*, confusion matrices are listed in Table III. The classifier accuracy was found to be 94.10% and 98.05%, respectively. The confusion matrices provide the evaluation data: true-positives (TP), true-negatives (TN),

TABLE III
CONFUSION MATRICES USING HOG FEATURE
VECTORS AND SVM CLASSIFIER.
(a) TEST SET *B*. (b) TEST SET *C*

| | | | |
|--------|----------|-----------|----------|
| | | Predicted | |
| | | Positive | Negative |
| Actual | Positive | 973 | 27 |
| | Negative | 81 | 909 |

| | | | |
|--------|----------|-----------|----------|
| | | Predicted | |
| | | Positive | Negative |
| Actual | Positive | 993 | 7 |
| | Negative | 32 | 968 |

TABLE IV
CONFUSION MATRICES USING HOG FEATURE
VECTORS AND NNET CLASSIFIER.
(a) TEST SET *B*. (b) TEST SET *C*

| | | | |
|--------|----------|-----------|----------|
| | | Predicted | |
| | | Positive | Negative |
| Actual | Positive | 985 | 1 |
| | Negative | 229 | 771 |

| | | | |
|--------|----------|-----------|----------|
| | | Predicted | |
| | | Positive | Negative |
| Actual | Positive | 999 | 1 |
| | Negative | 112 | 888 |

FP, and FN. The matrix indicates low number of both FP and FN. From the confusion matrix, the following performance metrics are computed: accuracy, precision, sensitivity, and specificity [50].

Table V shows the comparison of performance of HOG, gradient-orientation histogram, maximum gradient orientation, and edge pixels. In addition, the intensities of each sample and intensity histogram, which are simple intuitive feature vectors are also used for comparison. The poor performance of simple intuitive feature vectors is well documented in computer vision and it is observed that intensity values as a feature vector result in least accuracy and precision. We also use template matching for comparison with two matching criterion: 1) normalized sum of squared differences (NSSD) and 2) normalized cross-correlation coefficient (NCORR). The template matching result for each sample lies between 0 and 1. For NSSD, lower values (close to 0) indicate a strong match. For NCORR, higher values (close to 1) indicate a strong match. It is observed that for NSSD, when the threshold is increased from 0.09 to 0.10, the precision and specificity decreases while the sensitivity increases. Similarly, for NCORR, as the threshold is decreased from 0.96 to 0.95, the precision and specificity decreases while the sensitivity increases. HOG and gradient orientation histogram features outperform the other feature vectors. HOG features have highest sensitivity (97.3% and 99.3% for test sets *B* and *C*, respectively), which indicating least missing detections of hyperbolic signatures and maximum detection rate. HOG features also result in high accuracy (94.10% and 98.05% for test sets *B* and *C*, respectively).

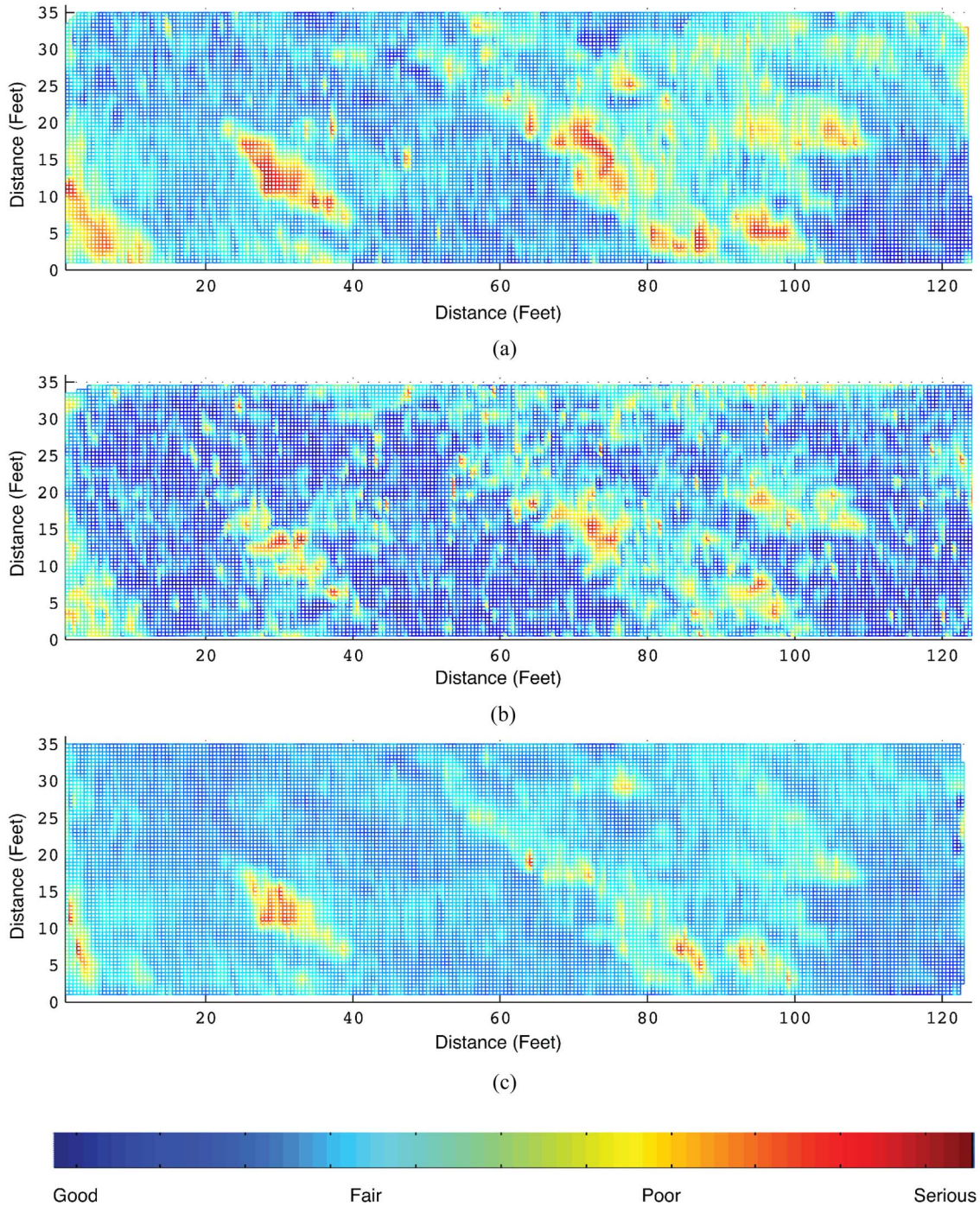


Fig. 13. Deterioration maps obtained using automated algorithm obtained from data collected using GPR system (a) GSSI SIR-20, (b) IDS Hi-Bright, and (c) using GSSI RADAN software obtained from data collected using GSSI SIR-20 GPR system. The deterioration map for the automated analysis (a) and (b) are comparable to the deterioration map using the RADAN software which uses human input and multiple stages of software analysis.

Neural networks (NNET) classifier can also be used to classify the hyperbolic signatures. Table IV lists the confusion matrices for test sets *B* and *C* obtained using HOG feature vectors and NNET classifier. The classifier accuracy was found to be 87.8% and 94.3%, respectively. Thus, SVM classifier outperforms the accuracy of NNET classifier. Moreover, the average time taken by the NNET classifier to classify hyperbolic signatures in both test sets is 24.9 ms whereas the SVM classifier takes 6.7 ms. Based on this quantitative analysis, we

use the SVM classifier using HOG feature vectors for the final detection algorithm. We use the MATLAB implementation of the SVM and NNET classifiers [51].

C. Rebar Detection and Localization

The trained SVM classifier is used to detect a rebar region and fit a hyperbola in each rebar region to find exact rebar location as described in Section III. The rebar detection rate

TABLE V
PERFORMANCE METRICS FOR SVM CLASSIFIER USING VARIOUS FEATURE VECTORS AND TEMPLATE MATCHING.
TEST SETS WERE CONSTRUCTED FROM TWO DIFFERENT BRIDGES

| Feature Vector | Accuracy (% correct) | | Precision (%) | | Sensitivity (%) | | Specificity (%) | |
|--|----------------------|--------------|---------------|--------------|-----------------|-------------|-----------------|-------------|
| | Test set 1 | Test set 2 | Test set 1 | Test set 2 | Test set 1 | Test set 2 | Test set 1 | Test set 2 |
| Intensity values | 72.7 | 64.8 | 75.62 | 67.25 | 67 | 57.7 | 78.4 | 71.9 |
| Intensity Histogram | 40.65 | 52.6 | 43.26 | 51.48 | 60 | 90.6 | 21.3 | 14.6 |
| Edge Pixels | 84.15 | 70.6 | 85.03 | 63.21 | 82.9 | 98.6 | 85.4 | 42.6 |
| Maximum gradient orientation | 83 | 89.45 | 78.8 | 90.88 | 90.3 | 87.7 | 75.7 | 91.2 |
| Gradient-orientation histogram | 91.55 | 98.1 | 90.78 | 98.78 | 92.5 | 97.4 | 90.6 | 98.8 |
| Histogram of Oriented Gradients | 94.1 | 98.05 | 91.45 | 96.88 | 97.3 | 99.3 | 90.9 | 96.8 |
| Template Matching NSSD (thresh = 0.09) | 79.65 | 68.95 | 85.68 | 77.11 | 71.2 | 53.9 | 88.1 | 84 |
| Template Matching NSSD (thresh = 0.10) | 73.75 | 76.35 | 66.83 | 70.7 | 94.3 | 90 | 53.2 | 62.7 |
| Template Matching NCCORR (thresh = 0.96) | 64.95 | 54.35 | 82.71 | 80 | 37.8 | 11.6 | 92.1 | 97.1 |
| Template Matching NCCORR (thresh = 0.95) | 57.4 | 75.35 | 54.2 | 68.63 | 95.6 | 93.4 | 19.2 | 57.3 |

TABLE VI
AVERAGE DETECTION RATE PER B-SCAN. THE DETECTION RATE INCLUDES THE SUCCESS OF BOTH REBAR REGION DETECTION AND HYPERBOLA FITTING

| Bridge | Length (feet) | No. of B-scans | Average detection rate (%) |
|--------|---------------|----------------|----------------------------|
| B | 124 | 18 | 91.5 \pm 1.23 |
| C | 335.5 | 11 | 92.45 \pm 2.38 |

includes both rebar region detection and hyperbola fitting. The rebar detection rate for Bridges *B* and *C* is 92.45% and 91.5%, respectively (Table VI). Ground truth for the rebar detection result is obtained using GSSI RADAN software with human interaction. For the ground truth data, false detections were removed and missing rebar detections were manually added in order to have a benchmark set.

D. Deterioration Maps

After analyzing all the B-scans in a bridge for rebars, the amplitude value at each rebar location is normalized and depth-corrected as described in Section III-E. The rebar locations and depth-corrected amplitudes are then used to obtain a deterioration map of the bridge deck. The regions are identified as serious, poor, fair, and good regions based on the signal amplitude (indicated by different colors). The lower signal amplitude indicates the deteriorated region, which is marked as serious or poor. Fig. 13(b) and (c) shows the maps obtained using automated algorithms for bridge *B* using data collected using GSSI SIR-20 and IDS Hi-Bright GPR, respectively. These deterioration maps are compared with the map obtained using rebar detection results from GSSI RADAN software, involving manual interaction [Fig. 13(a)]. From the deterioration maps obtained for Bridge *B* shown in Fig. 13, it is evident that the regions of deterioration identified by automated algorithms are comparable to those obtained by semi-automated methods requiring human interaction.

V. CONCLUSION

Automating the bridge deck inspection and evaluation process can save manpower and time, and also improve

repeatability of the results. In this paper, we have shown an automated rebar detection and localization algorithm to process large datasets and obtain deterioration maps with high accuracy. Rebar classification tests show the superiority of HOG features compared to other gradient and intensity-based feature vectors. The advantage of a machine learning approach is demonstrated where training from one bridge is used for not only for that bridge but also for two additional bridges. In this manner, the use of machine learning replaces tedious parameter tweaking and manual interaction with analysis software. The use of robotic measurements and automated analysis represents an exciting new approach that can enable in-field evaluation of bridge decks in a cost-effective manner.

ACKNOWLEDGMENT

The authors would like to thank researchers Dr. B. B. Basily, Dr. H. La, R. Lim, Dr. A. Maher, H. Parvardeh, P. Prassana, and Dr. J. Yi for their contributions in the robot planning, development, and data collection and would also like to thank Warren County Municipal Engineer J. Tate for support and access to a local bridge for repeated testing of the prototype robot.

REFERENCES

- [1] Y. P. Virmani and G. G. Clemena, "Corrosion protection-concrete bridges," U.S. Dept. Transp., Fed. Highw. Admin., McLean, VA, USA, Tech. Rep. FHWA-RD-98-088, Sep. 1998.
- [2] M. E. Henderson, G. N. Dion, and R. D. Costley, "Acoustic inspection of concrete bridge decks," *Proc. SPIE Nondestruct. Eval. Bridges Highw. III*, vol. 3587, pp. 219–227, Feb. 1999.
- [3] W. T. Scannell, A. A. Sohangpurwala, and M. Islam, *Assessment of Physical Condition of Concrete Bridge Components*, Concoor, Inc., Ashburn, VA, USA, 1996.
- [4] F. Romero, G. Roberts, and R. Roberts, "Evaluation of GPR bridge deck survey results used for delineation of removal/maintenance quantity boundaries on asphalt-overlaid, reinforced concrete deck," in *Proc. NDT Conf. Struct. Mater. Technol.*, Atlantic City, NJ, USA, pp. 23–30, 2000.
- [5] G. Roberts, R. Roberts, and A. Tarussov, "Identifying concrete deterioration using ground penetrating radar technology," in *Proc. Amer. Soc. Nondestruct. Test. Conf. (ASNT)*, Oct. 2001.

- [6] R. Parrillo, R. Roberts, and A. Haggan, "Bridge deck condition assessment using ground penetrating radar," in *Proc. 9th Eur. Conf. NDT*, Berlin, Germany, Sep. 2006, pp. 1–12.
- [7] H. M. La *et al.*, "Mechatronic systems design for an autonomous robotic system for high-efficiency bridge deck inspection and evaluation," *IEEE/ASME Trans. Mechatronics*, vol. 18, no. 6, pp. 1655–1664, Dec. 2013.
- [8] J. Hugenschmidt and P. Furholz, "ATRAS—An automated GPR system for data acquisition and storage for roads and bridges," in *Proc. 14th Int. Conf. Ground Penetrat. Radar (GPR)*, Shanghai, China, Jun. 2012, pp. 448–453.
- [9] A. Simi, G. Manacorda, and A. Benedetto, "Bridge deck survey with high resolution ground penetrating radar," in *Proc. 14th Int. Conf. Ground Penetrat. Radar (GPR)*, Shanghai, China, 2012, pp. 489–495.
- [10] X.-Q. He, Z.-Q. Zhu, Q.-Y. Liu, and G.-Y. Lu, "Review of GPR rebar detection," in *Proc. PIERS*, Beijing, China, pp. 804–813, Mar. 2009.
- [11] F. Soldovieri, R. Solimene, L. Lo Monte, M. Bavusi, and A. Loperte, "Sparse reconstruction from GPR data with applications to rebar detection," *IEEE Trans. Instrum. Meas.*, vol. 60, no. 3, pp. 1070–1079, Mar. 2011.
- [12] Y. Liu, M. Wang, and Q. Cai, "The target detection for GPR images based on curve fitting," in *Proc. 3rd Int. Congr. Image Signal Process. (CISP)*, vol. 6, Yantai, China, Oct. 2010, pp. 2876–2879.
- [13] V. Krause, I. Abdel-Qader, O. Abudayyeh, and S. Yehia, "An image segmentation algorithm for the detection of rebar in bridge decks from GPR scans," in *Proc. IEEE Int. Conf. Electro/Inf. Technol.*, Chicago, IL, USA, May 2007, pp. 114–119.
- [14] M. R. Shaw, S. G. Millard, T. C. K. Molyneaux, M. J. Taylor, and J. H. Bungey, "Location of steel reinforcement in concrete using ground penetrating radar and neural networks," *NDT&E Int.*, vol. 38, no. 3, pp. 203–212, Apr. 2005.
- [15] P. Gamba and S. Lossani, "Neural detection of pipe signatures in ground penetrating radar images," *IEEE Trans. Geosci. Remote Sens.*, vol. 38, no. 2, pp. 790–797, Mar. 2000.
- [16] W. Al-Nuaimy, Y. Huang, A. Eriksen, and V. T. Nguyen, "Automatic detection of hyperbolic signatures in ground-penetrating radar data," *Proc. SPIE*, vol. 4491, pp. 327–335, Nov. 2001. [Online]. Available: <http://dx.doi.org/10.1117/12.450177>
- [17] Z. W. Wang, M. Zhou, G. G. Slabaugh, J. Zhai, and T. Fang, "Automatic detection of bridge deck condition from ground penetrating radar images," *IEEE Trans. Autom. Sci. Eng.*, vol. 8, no. 3, pp. 633–640, Jul. 2011.
- [18] J. P. Lewis, "Fast normalized cross-correlation," *Vis. Interf.*, vol. 10, no. 1, pp. 120–123, 1995.
- [19] W. Al-Nuaimy *et al.*, "Automatic detection of buried utilities and solid objects with GPR using neural networks and pattern recognition," *J. Appl. Geophys.*, vol. 43, nos. 2–4, pp. 157–165, Mar. 2000.
- [20] S. Birkenfeld, "Automatic detection of reflexion hyperbolas in GPR data with neural networks," in *Proc. World Autom. Congr. (WAC)*, Kobe, Japan, Sep. 2010, pp. 1–6.
- [21] N. P. Singh and M. J. Nene, "Buried object detection and analysis of GPR images: Using neural network and curve fitting," in *Proc. Annu. Int. Conf. Emerg. Res. Areas Int. Conf. Microelectron. Commun. Renew. Energy (AICERA/ICMCR)*, Kanjirappally, India, Jun. 2013, pp. 1–6.
- [22] C. Cortes and V. Vapnik, "Support-vector networks," *Mach. Learn.*, vol. 20, no. 3, pp. 273–297, Sep. 1995.
- [23] B. Scholkopf and A. J. Smola, *Learning With Kernels: Support Vector Machines, Regularization, Optimization, and Beyond*. Cambridge, MA, USA: MIT Press, 2001.
- [24] E. Pasolli, F. Melgani, and M. Donelli, "Automatic analysis of GPR images: A pattern-recognition approach," *IEEE Trans. Geosci. Remote Sens.*, vol. 47, no. 7, pp. 2206–2217, Jul. 2009.
- [25] S. Shihab, W. Al-Nuaimy, and A. Eriksen, "Radius estimation for sub-surface cylindrical objects detected by ground penetrating radar," in *Proc. 10th Int. Conf. Ground Penetrat. Radar (GPR)*, vol. 1, Delft, The Netherlands, Jun. 2004, pp. 319–322.
- [26] N. Gucunski, F. Romero, S. Kruschwitz, R. Feldmann, and H. Parvardeh, "Comprehensive bridge deck deterioration mapping of nine bridges by nondestructive evaluation technologies," Iowa Dept. Transp., Fed. Highw. Admin., Ames, IA, USA, Tech. Rep. SPR-NDEB(90)–8H-00, 2011.
- [27] *RADAN, Version 7*, Geophys. Survey Syst., Inc., Salem, NH, USA, 2013. [Online]. Available: <http://www.geophysical.com/software.htm>
- [28] K. Maser, "Automated interpretation for sensing in situ conditions," *J. Comput. Civ. Eng.*, vol. 2, no. 3, pp. 215–238, Jul. 1988.
- [29] C. R. Carter, T. Chung, F. B. Holt, and D. G. Manning, "An automated signal processing system for the signature analysis of radar waveforms from bridge decks," *Can. Electr. Eng. J.*, vol. 11, no. 3, pp. 128–137, Jul. 1986.
- [30] K. Maser, "Bridge deck condition surveys using radar: Case studies of 28 New England decks," Transp. Res. Board, Nat. Res. Council, Washington, DC, USA, Tech. Rep. 00620406, 1991.
- [31] K. Maser and A. Rawson, "Network bridge deck surveys using high speed radar: Case studies of 44 decks," Transp. Res. Board, Washington, DC, USA, Tech. Rep. 00638500, 1993.
- [32] G. Roberts, *Bureau of Materials, and Research, Use of Ground Penetrating Radar to Delineate Bridge Deck Repair Areas*, New Hampshire Dept. Transp., Keene, NH, USA, 2002. [Online]. Available: <http://books.google.com/books?id=HgAYHAAACAAJ>
- [33] C. Barnes and J. Trotter, "Effectiveness of ground penetrating radar in predicting deck repair quantities," *J. Infrastruct. Syst.*, vol. 10, no. 2, pp. 69–76, 2004.
- [34] N. Dalal and B. Triggs, "Histograms of oriented gradients for human detection," in *Proc. IEEE Comput. Soc. Conf. Comput. Vis. Pattern Recognit.*, vol. 1, San Diego, CA, USA, Jun. 2005, pp. 886–893.
- [35] P. Dollár, S. Belongie, and P. Perona, "The fastest pedestrian detector in the west," in *Proc. Brit. Mach. Vis. Conf.*, London, U.K., 2010, pp. 68.1–68.11.
- [36] Q. Zhu, M.-C. Yeh, K.-T. Cheng, and S. Avidan, "Fast human detection using a cascade of histograms of oriented gradients," in *Proc. IEEE Comput. Soc. Conf. Comput. Vis. Pattern Recognit.*, vol. 2, New York, NY, USA, 2006, pp. 1491–1498.
- [37] W. Zhang, G. Zelinsky, and D. Samaras, "Real-time accurate object detection using multiple resolutions," in *Proc. IEEE 11th Int. Conf. Comput. Vis.*, Rio de Janeiro, Brazil, 2007, pp. 1–8.
- [38] X. Wang, T. Han, and S. Yan, "An HOG-LBP human detector with partial occlusion handling," in *Proc. IEEE 12th Int. Conf. Comput. Vis.*, Kyoto, Japan, 2009, pp. 32–39.
- [39] V. Ferrari, L. Fevrier, F. Jurie, and C. Schmid, "Groups of adjacent contour segments for object detection," *IEEE Trans. Pattern Anal. Mach. Intell.*, vol. 30, no. 1, pp. 36–51, Jan. 2008.
- [40] P. Dollár. (Mar. 2014). *Piotr's Computer Vision MATLAB Toolbox (PMT)*. [Online]. Available: <http://vision.ucsd.edu/~pdollar/toolbox/doc/index.html>
- [41] Y. Pang, H. Yan, Y. Yuan, and K. Wang, "Robust CoHOG feature extraction in human-centered image/video management system," *IEEE Trans. Syst., Man, Cybern. B, Cybern.*, vol. 42, no. 2, pp. 458–468, Apr. 2012.
- [42] Y. Xu *et al.*, "Detection of sudden pedestrian crossings for driving assistance systems," *IEEE Trans. Syst., Man, Cybern. B, Cybern.*, vol. 42, no. 3, pp. 729–739, Jun. 2012.
- [43] Y. Pang, K. Zhang, Y. Yuan, and K. Wang, "Distributed object detection with linear SVMs," *IEEE Trans. Cybern.*, vol. 44, no. 11, pp. 2122–2133, Nov. 2014.
- [44] M. A. Aziz, J. Niu, X. Zhao, and X. Li, "Efficient and robust learning for sustainable and reacquisition-enabled hand tracking," *IEEE Trans. Cybern.*, DOI: 10.1109/TCYB.2015.2418275.
- [45] S. Birkenfeld, "Automatic detection of reflexion hyperbolas in gpr data with neural networks," in *Proc. World Autom. Congr. (WAC)*, Kobe, Japan, 2010, pp. 1–6.
- [46] M. A. Fischler and R. C. Bolles, "Random sample consensus: A paradigm for model fitting with applications to image analysis and automated cartography," *Commun. ACM*, vol. 24, no. 6, pp. 381–395, Jun. 1981.
- [47] P. D. Kovesi. (Mar. 2014). *MATLAB and Octave Functions for Computer Vision and Image Processing, Centre for Exploration Targeting, School of Earth and Environment, University of Western Australia*. [Online]. Available: <http://www.peterkovesi.com/matlabfnsl/>, accessed Sep. 2015.
- [48] C. L. Barnes, J.-F. Trotter, and D. Forgeron, "Improved concrete bridge deck evaluation using GPR by accounting for signal depth-amplitude effects," *NDT&E Int.*, vol. 41, no. 6, pp. 427–433, 2008.
- [49] F. Romero, M. Premo, D. Severns, and J. G. Diehl, "Interstate-80 corridor ground-penetrating radar bridge assessments: Deterioration mapping of asphalt-overlaid and polymer concrete-overlaid, reinforced concrete decks in Elko county, Nevada," Transp. Res. Board, Washington, DC, USA, Tech. Rep. 01123120, 2009.
- [50] T. Fawcett, "An introduction to ROC analysis," *Pattern Recognit. Lett.*, vol. 27, no. 8, pp. 861–874, 2006.
- [51] *MATLAB Neural Network Toolbox, Version 8.1.0 (R2013a)*, MathWorks Inc., Natick, MA, USA, 2013.



Parneet Kaur received the B.E. degree in electronics and communication engineering from the Dayananda Sagar College of Engineering, Visvesvaraya Technological University, Belgaum, India, in 2007, and the M.S. degree in electrical and computer engineering from Rutgers University, Piscataway, NJ, USA, in 2013. She is currently pursuing the Ph.D. degree in electrical and computer engineering with Rutgers University.

From 2007 to 2009, she was a Software Engineer with Robert Bosch Engineering and Business Solutions Ltd., Bangalore, India, where she developed software for real-time embedded systems deployed in automobile platforms. From 2012 to 2013, she was a Graduate Research Assistant with the Department of Electrical and Computer Engineering, and the Center for Advanced Infrastructure and Transportation, Rutgers University. She was involved in the development of the Robotics Assisted Bridge Inspection Tool (RABIT) funded by the Federal Highway Administration. Her current research interests include computer vision, machine learning, and pattern recognition.

Ms. Kaur was a Team Member Recipient of the 2014 American Society of Civil Engineers (ASCE) Charles Pankow Award for Innovation for the RABIT project.



Kristin J. Dana received the B.S. degree in computer science and electrical engineering from Cooper Union, New York, NY, USA, in 1990, the M.S. degree in electrical engineering and computer science from the Massachusetts Institute of Technology, Cambridge, MA, USA, in 1992, and the Ph.D. degree in electrical engineering from Columbia University, New York, in 1999.

She is an Associate Professor with the Department of Electrical and Computer Engineering, Rutgers University, Piscataway, NJ, USA. She is the Inventor of the Texcam texture camera for convenient measurement of reflectance and texture. She is also a member of the Rutgers Center for Cognitive Science and the Graduate Faculty of the Computer Science Department. From 1992 to 1995, she was a Research Staff with Sarnoff Corporation, Princeton, NJ, USA, developing real-time motion estimation algorithms for applications in defense, biomedicine, and entertainment industries. Her current research interests include computer vision, such as computational photography, machine learning, illumination modeling, texture and reflectance, bioimaging, motion estimation, optical devices, optimization in vision, and applications of robotics.

Dr. Dana was a recipient of the National Science Foundation Career Award for a program investigating surface science for vision and graphics in 2001, and a Team Member Recipient of the Charles Pankow Innovation Award in 2014 from the ASCE.



Francisco A. Romero received the B.S. degree in petroleum engineering from New Mexico Tech, Socorro, NM, USA, in 1984, and the M.S. degree in civil/structural engineering from the University of Kansas, Lawrence, KS, USA, in 1992.

He is the President and the Owner of Romero nondestructive test (NDT)&E, LLC, Glen Gardner, NJ, USA, providing professional ground penetrating radar (GPR)/NDT&E services, such as condition assessment, general near-surface geophysical applications, high speed pavement condition assessment, damage prevention, and structural evaluation. He also provides professional GPR/non-destructive evaluation (NDE) consulting, training, and business development services with expertise related to civil/infrastructure NDT applications, and is active on the GPR TEAM Board of Directors. Since 1993, he has been continuously using GPR and other NDE methods for a variety of commercial and public projects, applications, pilot studies and research; mostly in structural engineering and transportation infrastructure condition assessment of buildings, bridges, highway pavements, tunnels, dams, buildings, and airport runways and tarmacs. His NDT/geophysics research began as an oilfield acoustic and nuclear wireline logging engineer, and his materials testing and research background includes the full complement of field, laboratory and batch plant construction materials testing and inspection, such as concrete, soils/aggregates, asphalt, with some metals and geophysics/geotechnical work.



Nenad Gucunski received the B.S.E. degree in civil engineering from the University of Zagreb, Croatia, in 1979, and the M.S. and Ph.D. degrees in civil engineering from the University of Michigan, Ann Arbor, MI, USA, in 1983 and 1991, respectively.

He is a Professor and the Chairman of Civil and Environmental Engineering, Rutgers University, Piscataway, NJ, USA. He is the Director of Infrastructure Condition Monitoring Program with Rutgers' Center for Advanced Infrastructure and Transportation. His expertise is in nondestructive test (NDT)/NDE of transportation infrastructure and has published over 150 publications on various aspects of the NDE/NDT technologies development, application, and automation. He is/was leading a number of important infrastructure related research projects, including the National Institute of Standards and Technology-Technology Innovation Program, Automated Nondestructive Evaluation and Rehabilitation System project on the development of a systems of devices for local and global NDE assessment and rehabilitation of bridges, Strategic Highway Research Project 2 project on NDE for Bridge Decks, Federal Highway Administrations Long Term Bridge Performance Program, and several other projects for state and federal government and industry.

Dr. Gucunski was a recipient of the 2014 ASCE Charles Pankow Award for Innovation for the development of Robotics Assisted Bridge Inspection Tool for bridge decks. He is an Active Member of a number of societies. He serves as the Chair of the ASCEs Geophysical Engineering Committee.